© 2005 Society for Industrial and Applied Mathematics

# MULTISCALE TWO-DIMENSIONAL MODELING OF A MOTILE SIMPLE-SHAPED CELL[*]

B. RUBINSTEIN[†], K. JACOBSON[‡], AND A. MOGILNER[†]

**Abstract.** Cell crawling is an important biological phenomenon underlying coordinated cell movement in morphogenesis, cancer, and wound healing. In recent decades the process of cell crawling has been experimentally and theoretically dissected into further subprocesses: protrusion of the cell at its leading edge, retraction of the cell body, and graded adhesion. A number of one-dimensional (1-D) models explain successfully a proximal-distal organization and movement of the motile cell. However, more adequate two-dimensional (2-D) models are lacking. We propose a multiscale 2-D computational model of the lamellipodium (motile appendage) of a simply shaped, rapidly crawling fish keratocyte cell. We couple submodels of (i) protrusion and adhesion at the leading edge, (ii) the elastic 2-D lamellipodial actin network, (iii) the actin-myosin contractile bundle at the rear edge, and (iv) the convection-reaction-diffusion actin transport on the free boundary lamellipodial domain. We simulate the combined model numerically using a finite element approach. The simulations reproduce observed cell shapes, forces, and movements and explain some experimental results on perturbations of the actin machinery. This novel 2-D model of the crawling cell makes testable predictions and posits questions to be answered by future modeling.

**Key words.** cell motility, actin, lamellipodium, free boundary problem, keratocyte

**AMS subject classifications.** 92C37, 92C40, 92C15, 37N25

**DOI.** 10.1137/04060370X

**1. Introduction.** Cell crawling [5] is an important part of many biological processes such as wound healing, immune response, cancer, and morphogenesis. Almost all crawling cells move by using dynamic actin machinery to power a simple mechanical cycle [1]: first, the polarized actin network grows at the front and pushes out the cell's leading edge; next, the cell strengthens its adhesions at the leading edge and weakens them at the rear edge; finally, the cell pulls up its rear. Answers to the question of how the mechanochemical events driving this cycle determine cell shape and cell movements have proven elusive due to the large number of proteins involved in cell locomotion, as well as the intricacy of the intracellular control system.

A well-defined model system is crucial for obtaining answers about this *relationship between actin dynamics and cell shape and movements*. Our cells of choice are *fish epidermal keratocytes* which crawl on surfaces with remarkable speed and persistence while almost perfectly maintaining their characteristic fan-like shape [12] (Figure 1). Keratocyte cells, streamlined for migration, offer powerful advantages for modeling. In these cells the steps of protrusion, graded adhesion, and retraction are continuous and simultaneous, and there is clear spatial separation between them. Protrusion and adhesion are confined to the leading edge, while retraction occurs at the rear and the
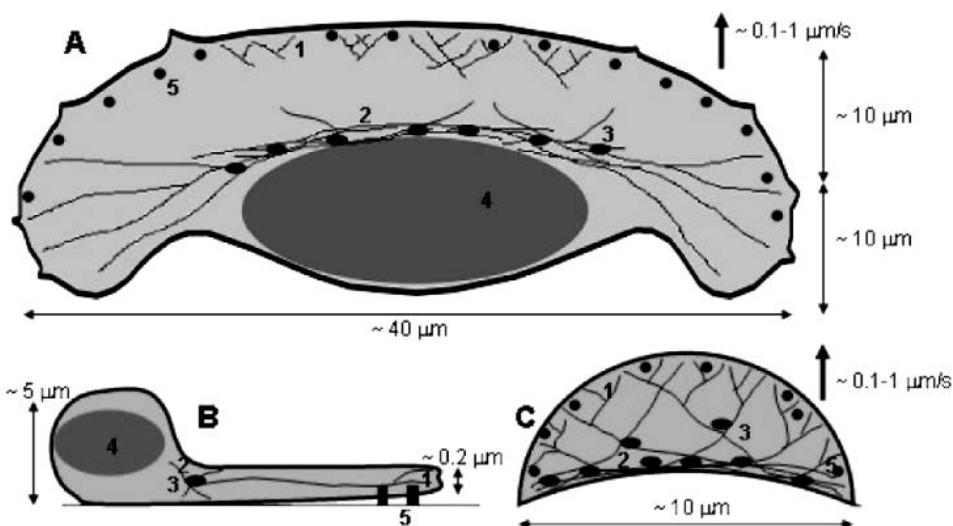
FIG. 1. *Schematic diagrams of a fish keratocyte cell as seen from above* (A) *and from the side* (B) *and of a migrating lamellipodial fragment as seen from above* (C). *Typical shapes and dimensions are shown: 1. branching actin network in the lamellipodium; 2. bipolar actin-myosin bundle at the rear of the lamellipodium; 3. myosin clusters; 4. cell body; 5. adhesion complexes. Note the concave shapes of the leading (top) and rear (bottom) edges of the lamellipodial fragment and the characteristic crescent shape of the lamellipodium.*

extreme lateral edges [32, 2]. The fan-like shape of a keratocyte is likely to represent the basic shape of the crawling cell in its pure form, determined solely by the actin network dynamics.

The *lamellipodium* is the front, advancing part of the keratocyte and is the basic engine for crawling [27, 25]. It is a flat, leaf-like extension filled with a dense actin network. It is only a few tenths of a micrometer thick but is several tens of micrometers wide and about 10 micrometers long (Figure 1). The cell body, containing the cell nucleus and other organelles, appears to be a mechanically passive structure in the crawling—pulled forward entirely by the lamellipodial action. Recently, significant progress has been made in understanding the molecular events of protrusion, adhesion, and retraction, as well as the structural organization of the lamellipodial actin network [27, 18, 32]. Moreover, lamellipodial fragments separated from the cell body have been observed to exhibit autonomous motility and whole-cell shape characteristics [34]. These observations suggest that a two-dimensional (2-D) model able to explain the dynamics of the flat autonomous lamellipodium would be very useful for understanding the basic process of cell crawling.

While a number of one-dimensional (1-D) models have examined various aspects of cell motility [8, 23, 11], these models cannot properly address the issue of cell shape. Therefore a 2-D model is required. Very few studies quantitatively address the lamellipodial shape. (See [30] for an interesting 2-D model motivated physically, rather than biologically.) The graded radial extension (GRE) model sheds light on kinematic principles underlying keratocyte shape [17]. This model, accompanied by experimental observations, demonstrates that extension/retraction is locally normal to the cell boundary and that the rate of extension/retraction is graded, decreasing from the center to the sides of the cell. It also shows that the 2-D steady-state cell shape evolves as a function of the extension/retraction rates. The GRE model

does not examine the role feedback plays in the relationship between cell shape and actin dynamics. Another combined experimental and theoretical study elucidates the dynamic feedback between the actin polymerization at the cell's leading edge and the shape of that edge [12]. This same study, however, does not examine the behavior at the rear and sides of the cell. A 2-D computational model simulates the forces, shapes, and movements of nematode sperm cells [4]. These cells' amoeboid motility is very similar to that of the actin-based cells [5]. However, the underlying physics of protrusion, retraction, and adhesion are different and very peculiar. The model we present here borrows from the ideology and methodology of the nematode sperm model, although specifics of the two models are different.

In this paper, we propose a self-consistent 2-D model of the mechanochemistry of the keratocyte lamellipodial fragment (referred to below simply as lamellipodium). We analyze this model mathematically and numerically. The model elucidates principles underlying self-organization of the lamellipodium, provides a dynamic mechanism for the GRE model, and explains the nature of the stability and persistence of cell crawling. To our knowledge, this is the first 2-D mathematical model combining the mechanics of protrusion, graded adhesion, and retraction with those of actin turnover. We show how this coupling generates stable, steady, rapid migration of the actin-based cells.

The layout of the paper is as follows. In the next section, we describe relevant experimental data and outline a qualitative model of the lamellipodium. Then in sections 3–6 we propose submodels for protrusion/adhesion, myosin driven retraction, 2-D lamellipodial elasticity, and actin turnover and transport, respectively. We report the results of the numerical simulations of the model in section 7 and apply the model to simulate keratocyte turning behavior in section 8. We conclude with a discussion of the model's predictions and biological implications in section 9.

## 2. Qualitative model of the lamellipodial dynamics.

**2.1. Protrusion and actin dynamics.** Protrusion is the most well-studied subprocess of motility. The following *dendritic nucleation model* describes the growth of actin network, which is the basis of protrusion. Although the model is still not confirmed in all its details, it is accepted in general [27]. First, Arp2/3 protein complex causes nucleation and branching of nascent *actin filaments* (F-actin) from the sides of existing actin filaments at the leading edge of the lamellipodium (Figure 1). Actin filaments are polar: *pointed ends* of newly formed filaments are capped and stabilized at a branching point, while their free *barbed ends* elongate, pushing the membrane at the leading edge forward, until they are capped by capping proteins. Thus the lamellipodial actin network has a branched organization; Arp2/3 complex localizes to the Y-junctions that give birth to daughter filaments oriented at about 70° to the mother filament (Figure 1). The network is further reinforced by crosslinking proteins.

*Actin monomers* (G-actin) are used for the elongation of the uncapped barbed ends. These monomers are produced in the process of disassembly at the opposite, pointed ends. This process is mediated by proteins of the ADF/cofilin family that are likely to accelerate either the uncapping of Arp2/3 bound minus ends, the severing of the filaments, or both. These proteins then accelerate disassembly of the minus ends across the lamellipodium. As a result, actin network density decreases exponentially from the front to the rear of the lamellipodium (for a review, see [24, 27]). Newly depolymerized actin monomers are sequestered by ADF/cofilin proteins, but they rapidly exchange this sequestered agent for one of two other important actin binding proteins—profilin and thymosin. At the same time they bind ATP, which is used

as an energy source in actin turnover [24, 27]. Actin-thymosin complexes cannot polymerize. This pool is maintained by the cell as a "backup," while actin-profilin complexes attach to the uncapped barbed ends. Actin-thymosin and actin-profilin are delivered from the depolymerization sites to the leading edge by diffusion, probably augmented by a cytoplasmic fluid-phase flow in the lamellipodium [24, 37].

Protrusion involves generating pushing forces at the front of the lamellipodium. Most likely, these forces are generated by elastic polymerization ratchet. In this process actin filaments and the cell membrane bend away from each other, actin monomers intercalate into the gap between the filament tip and the membrane, assembling onto the tip, and the elongated bent filaments push the membrane forward with elastic force [20, 21, 25].

**2.2. Adhesion.** Although the protrusion phase does not, per se, require contact with the substrate, adhesion is necessary for stabilization of the protrusion and can influence both its final shape and amplitude [7]. In the major part of the keratocyte lamellipodium, the actin network is stationary with respect to the substratum, while the cell moves forward [32]. The firm adhesion of the actin lamellipodial network to the substratum makes the forward motion possible [18]. This adhesion is mediated by attachments consisting of transmembrane integrin molecules bound simultaneously to substratum and cytoskeletal protein complexes (containing vinculin, talin, and other important proteins), which in turn bind to actin filaments. Mapping of the attachments between the lamellipodium and the substratum shows higher density of adhesion molecules at the front parts of the lamellipodium [18] (Figure 1). On a molecular level, how the attachments localize to the leading edge is unclear, although multiple integrin-mediated adhesion pathways are known to feed back on this localized protrusion activity [14]. For example, recruitment of Arp2/3 complex (crucial for protrusion) to vinculin (crucial for adhesion) might be one mechanism through which protrusion is coupled to integrin-mediated adhesion, providing a direct explanation for the potentiation effect of adhesion on protrusion [7].

**2.3. Retraction.** Pulling up the rear of the lamellipodium involves *contractile forces*. *Myosin*-driven contraction of the actin network generates the necessary forces [32, 34]. The model introduced in this paper suggests that actin disassembly weakens the network in the posterior region of the lamellipodium. This allows myosin-powered collapse of the largely isotropic lamellipodial actin network into a *bipolar actin-myosin bundle* at the very rear of the lamellipodium (Figure 1). Subsequent (muscle-like) sliding contraction of the bundle pulls lamellipodial actin filaments into the bundle, advancing the rear boundary of the lamellipodium forward. The detailed 1-D model of this actin-myosin contraction of the proximal-distal transect of the central part of the lamellipodium was reported in [23]. Active actin-myosin contraction is confined to a narrow, rear part of the lamellipodium [32, 34]. Probably the bulk of the lamellipodium reacts to this contraction only through passive elastic forces.

**2.4. The model.** The model is based on the following seven assumptions. Three factors can inhibit protrusion: membrane resistance, recycling of monomeric actin from the rear to the front, and adhesion strength. In keratocytes, the resistance is relatively weak [12], and we will assume here that the (i) *protrusion rate is locally normal to the leading edge and proportional to the local concentration of G-actin (either free or bound to profilin)* [24]. This assumption is implicitly based on another assumption, namely, that there is no rearward slippage of the actin network at the leading edge.

Without firm adhesion to the substratum, newly grown sheets of actin network buckle and drift backward [3]. There is evidence that the contractile forces are transmitted across the lamellipodium [10]. These forces either can break the nascent adhesions or can reinforce tight filamin binding and restrict integrin-dependent transient membrane protrusion [6]. These processes would decrease the density of adhesions and the rate of protrusion. We assume that (ii) *the actin-myosin contractile forces deform the elastic actin network of the lamellipodium and diminish adhesion density and protrusion at the leading edge.* Therefore, (iii) *the protrusion rate is an increasing function of the adhesion density, which, in turn, is a decreasing function of the magnitude of the local elastic deformation force.* We also assume that this force leads to a partial disassembly of the nascent F-actin so that (iv) *the density of F-actin at the leading edge is a decreasing function of the magnitude of the local elastic deformation force.*

We assume that (v) *the only limiting factor in determining lamellipodium size is a constant number of adhesion molecules which are distributed evenly along the leading edge.* That is, densities of Arp2/3 complexes, capping proteins, and myosin are assumed to be constant and independent of the lamellipodial shape and size. According to this assumption, if the lamellipodium grows too much, the density of the adhesions along the leading edge decreases. Meanwhile, the myosin-generated force deforming and disassembling the adhesions does not change, so the protrusion and F-actin density at the leading edge decrease. As a result, while the rear edge retraction does not change, the leading edge advances less, resulting in decreased lamellipodial area. Although this assumption gives qualitative insights as to how the total area of the lamellipodium is controlled, a quantitative model is needed to understand how the shape is controlled.

Other possible assumptions can explain the stability of the lamellipodial area. One such assumption is that the total amount of Arp2/3 is the limiting factor in determining the area's size. In this case, area growth would deplete Arp2/3 density. Depleted Arp2/3 density weakens the F-actin network, enabling myosin to collapse it more effectively, decreasing the area. Much more experimental data than is now available is needed to better understand the nature of the processes regulating the lamellipodial area.

Our remaining assumptions are as follows: (vi) *the lamellipodial network disassembles at a constant rate*; and (vii) *there exists a constant critical low F-actin density at which the actin network collapses into the actin-myosin bundle, determining the rear edge of the lamellipodium.*

In the next four sections we demonstrate that expressing these assumptions in mathematical terms is sufficient to reproduce the shape and movement of the lamellipodium. The general idea of the model is as follows. The actin-myosin contraction at the rear edge generates forces which deform the 2-D elastic lamellipodial sheet, straining the adhesions along the leading edge. We will demonstrate that the contraction forces increase from the center to the sides. As a result, adhesion strain also increases from the center to the sides. This gradually inhibits protrusion toward the sides of the cell, effectively bending the leading edge into its characteristic concave shape. The rear edge assumes a correspondingly concave shape, although less curved, defined by locations of critical low actin density. Monomeric actin reactions, diffusion, and convection create an actin gradient from the rear to the front of the cell. The gradient maintains sufficiently high G-actin concentration for protrusion at the leading edge. We neglect slippage and viscoelastic deformations at the lamellipodial sides. We have also neglected the continuous actin-myosin bundle distribution across

TABLE 1
*Model variables.*

| Symbol | Meaning | Units |
|---|---|---|
| $V$ | protrusion rate | $\mu$m/sec |
| $a$ | G-actin or G-actin-profilin concentration | $\mu$M |
| $g$ | force dependent factor | $\mu$M |
| $\mathbf{x}$ | 2-D coordinate | nondimensional |
| $F_e$ | magnitude of the elastic force at the leading edge | pN/$\mu$m |
| $F_{cr}$ | critical force constant at which protrusion stops | pN/$\mu$m |
| $L_{le}$ | length of the leading edge | $\mu$m |
| $f$ | F-actin density along the leading edge | filaments/$\mu$m |
| $m(x,t)$ | myosin density along the rear edge | molecules/$\mu$m |
| $r(x,t)$ | right-oriented filament density along the rear edge | filaments/$\mu$m |
| $l(x,t)$ | left-oriented filament density along the rear edge | filaments/$\mu$m |
| $v_m$ | velocity of myosin clusters along the rear edge | $\mu$m/sec |
| $v_r$ | velocity of right-oriented filaments along the rear edge | $\mu$m/sec |
| $v_l$ | velocity of left-oriented filaments along the rear edge | $\mu$m/sec |
| $\Pi$ | elastic potential energy | nN$\cdot\mu$m |
| $\sigma$ | elastic stress | nN/$\mu$m |
| $\epsilon$ | elastic strain | nondimensional |
| $\mathbf{u}$ | elastic displacement | $\mu$m |
| $\mathbf{T}$ | traction forces at the rear | nN/$\mu$m |
| $b$ | G-actin-thymosin concentration | $\mu$M |
| $a$ | free G-actin or G-actin-profilin concentration | $\mu$M |
| $\beta$ | thymosin concentration | $\mu$M |
| $\mathbf{V}_c$ | convection velocity | $\mu$m/sec |
| $P$ | hydrostatic pressure | Pa |
| $K$ | permeability | $\mu$m$^2$ |
| $\phi$ | porosity | nondimensional |

part of the lamellipodial rear. It remains to be seen how this affects our model's predictive power. Despite these limitations, however, the quantitative analysis of this model is a necessary first step in developing a comprehensive theory of cell motility.

**3. Mathematical model of protrusion at the leading edge.** Variables and parameters of the submodels introduced in this and the next sections are listed in Tables 1 and 2, respectively. We approximate the effective rate of protrusion at the leading edge as

$$(3.1) \qquad\qquad V(\mathbf{x}) = \delta k_{on} a(\mathbf{x}) \cdot g(\mathbf{x}),$$

neglecting the weak membrane resistance to actin polymerization and the slow disassembly rate at the barbed end. In this equation $\delta$ is the half-size of an actin monomer and $k_{on}$ is the assembly constant. At location $\mathbf{x} = (x, y)$ along the leading edge $a(\mathbf{x})$ is the local concentration of ATP-G-actin, either free or in complex with profilin. In order to establish the vectorial coordinate system, at each computational step we find a rectangle bounding the lamellipodial domain. The center of this rectangle is the origin of the coordinate system. The $x$-axis is taken as that perpendicular to the direction of motion. Similarly, the $y$-axis is parallel to the direction of movement, with positive

| Symbol | Meaning | Value |
|---|---|---|
| $\delta$ | half-size of actin monomer | 2.7 nm [24] |
| $k_{on}$ | barbed end assembly rate | 11.6 $\mu$M$^{-1}$sec$^{-1}$ [24] |
| $F_0$ | force constant | $10^3$ pN/$\mu$m |
| $F_{cr}^0$ | critical force constant | $10^3$ pN/$\mu$m |
| $L$ | spatial scale | 10 $\mu$m |
| $f_{cr}$ | critical F-actin density at which the actin network collapses | 100 filaments/$\mu$m |
| $f_0$ | maximal (force-free) F-actin density | 200 filaments/$\mu$m |
| $\gamma_b$ | F-actin disassembly rate in the bundle | 0.2 sec$^{-1}$, assumed |
| $\gamma_m$ | myosin disassembly rate in the bundle | 0.2 sec$^{-1}$, assumed |
| $\gamma_l$ | F-actin disassembly rate in the lamellipodium | 0.02 sec$^{-1}$ [24] |
| $n_m$ | myosin source at the rear | not specified |
| $n_0$ | F-actin source at the rear | not specified |
| $\epsilon_{1,2}$ | nondimensional actin, myosin velocities at the rear | $\ll 1$ |
| $Y$ | Young's modulus | 10 kPa [28] |
| $D$ | G-actin diffusion coefficient | 10 $\mu$m$^2$/sec [24] |
| $k_1, k_2, k_1', k_2'$ | G-actin reaction rates | 1/sec [24] |
| $\eta$ | water viscosity | 1 cPoise |
| $d$ | actin filament diameter | 5 nm |
| $\nu$ | geometric conversion factor | 500 $\mu$M$^{-1}\mu$m$^{-2}$ [24] |

direction corresponding to the direction of movement. Expression $\delta k_{on} a(\mathbf{x})$ is the free polymerization rate. The protrusion rate is given by modifying the polymerization rate with the nondimensional factor:

$$(3.2) \qquad g(\mathbf{x}) = \begin{cases} \exp(-F_e(\mathbf{x})/F_0) - \exp(-F_{cr}/F_0), & F_e(\mathbf{x}) < F_{cr}, \\ 0, & F_e(\mathbf{x}) \geq F_{cr}, \end{cases}$$

$$(3.3) \qquad F_{cr} = F_{cr}^0 \frac{L}{L_{le}}.$$

This phenomenological factor captures the mediating effects of the elastic and adhesive forces at the leading edge. We assume that when the critical force, $F_{cr}$, is reached, all nascent protrusions are lifted off the substratum and recede, stalling effective protrusion. This critical force is determined by the effective density of attachments. Formula (3.3) reflects our assumption that the total number of adhesions is distributed uniformly along the leading edge whose length is $L_{le}$. When the force deforming the attachments is subcritical, we assume effective protrusion is slowed exponentially (3.2). This assumption stems from a frequently observed exponential dependence of the adhesion breakage rate on the force [9]. $F_0$, $F_{cr}^0$, and $L$ are phenomenological parameters. The velocity profile $V(\mathbf{x})$ is an output calculated at each computational step using computed values of G-actin concentration and elastic force (see below).

We describe the advancing lamellipodium geometrically by attributing the normal protrusion velocity to every point on the leading edge. This is in accordance with the GRE model [17]. Figure 2 illustrates this using the sample parabolic force distribution, $F_e = c_1 + c_2 x^2$, along the leading edge. In this force expression, $c_1$ and $c_2$ are positive constants and $x$ is the 1-D lateral coordinate. The force affects the magnitude of
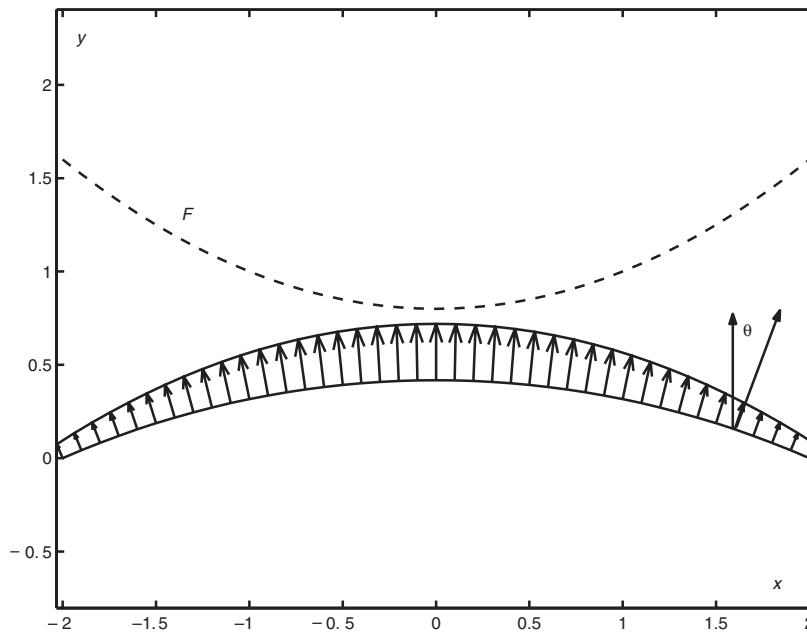
FIG. 2. *The protrusion (arrows) is graded along the leading edge (described by the function $y(x)$) by the elastic deformation force (dashed) according to (3.1)–(3.2). The initial shape of the leading edge is shown with the lower solid curve. In a short time interval, the edge advances and deforms into the upper solid curve. The slope of the edge is measured by the angle $\theta$, which is the function of the $x$-coordinate. The $x$-axis is directed from side to side of the cell; the $y$-axis is in the direction of migration.*

the local normal protrusion velocity $V(x)$ so that the protrusion speed decreases symmetrically from the edge's center to its sides. The shape shown evolves over a short time interval. For stationary rates of protrusion, a steady and stable concave shape evolves [17, 12]. The slope of such a shape is given by the formula $\theta(x) = \arccos(V(x)/V(0))$.

Finally, we assume that the effective density of F-actin along the leading edge is graded by the same force-dependent factor as the protrusion rate:

$$(3.4) \qquad\qquad f(\mathbf{x}) = f_{cr} + (f_0 - f_{cr})g(\mathbf{x}),$$

where $g(\mathbf{x})$ is as defined in (3.2). In this case $f_{cr}$ represents the critical low density of the actin network; at this density myosin can collapse the network into a bipolar bundle. We assume this critical density is reached at the same critical deformation force at which protrusion stops. The parameter $f_0$ is the maximal density of the actin network, attained when the leading edge is not deformed. We rationalize formula (3.4) due to the possibility that the deformation destroys some of the nascent actin network (depending on the force magnitude). There is also a possibility that F-actin density is force-independent and graded by kinematic effects of the lateral flow [12]; this possibility will be examined elsewhere.

**4. Mathematical model of actin-myosin contraction at the rear.** As explained above, we assume that all actin-myosin contraction occurs at the rear boundary of the lamellipodium. Therefore the corresponding submodel of actin-myosin contraction is 1-D. This is a very strong assumption; in later versions of the model

it will be changed to incorporate a continuous distribution of bundles throughout the cell. A pioneering quantitative model for the 1-D actin-myosin contraction was developed in [15] but is not directly applicable to the actin-myosin bundle in the lamellipodium. We suggest an alternative model of the actin-myosin contraction. In this 1-D model, we consider active, contractile, sliding elements (or bundles). These elements are composed of actin and myosin and are distributed along the rear edge of the lamellipodium (Figure 3). At the end of the next section, we explain how the contractile forces generated by these sliding elements are applied to the lamellipodial network: deforming the network, breaking the crosslinks, and pulling network actin filaments into the contractile bundle.
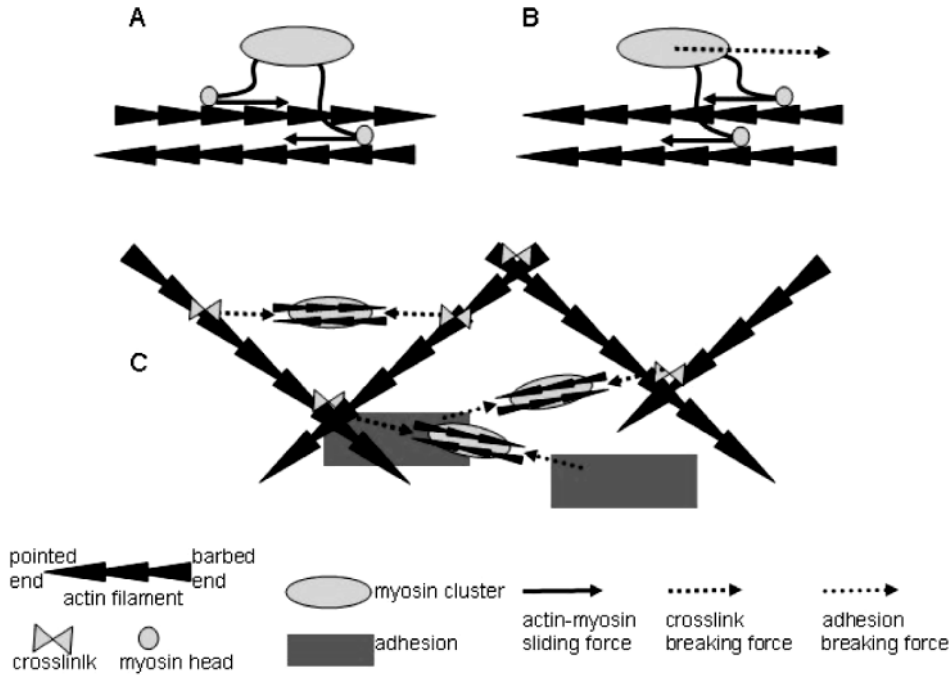


FIG. 3. *A myosin cluster interacts through multiple motor domains with bundle and network actin filaments. Active forces are generated through bundle actin-myosin sliding. Resistive forces arise from breaking crosslinks between myosin clusters and bundle actin filaments on the one hand and between network filaments and adhesions on the other hand.* A. *A contractile element at the center of the rear edge.* B. *A contractile element at the right of the rear edge.* C. *Force balance at the rear of the lamellipodium.*

We describe the actin-myosin bundle with three densities: the density of myosin clusters is denoted by $m(x, t)$; the density of actin filaments whose barbed ends are oriented to the right is denoted by $r(x, t)$; and $l(x, t)$ gives the density of those actin filaments whose barbed ends are oriented to the left. Time is given by $t$, and $x$ is the 1-D arc length coordinate along the bundle. We assume a bundle of constant length: $-L \leq x \leq L$; $x = 0$ corresponds to the center of the bundle. These densities are governed according to

$$(4.1) \qquad \frac{\partial r}{\partial t} = n_r(x) - \gamma_b r + \frac{\partial}{\partial x}(v_r r),$$

$$(4.2) \qquad \frac{\partial l}{\partial t} = n_l(x) - \gamma_b l - \frac{\partial}{\partial x}(v_l l),$$

$$(4.3) \qquad \frac{\partial m}{\partial t} = n_m - \gamma_m m - \frac{\partial}{\partial x}(v_m m),$$

where $\gamma_b$ and $\gamma_m$ are the constant rates of actin disassembly within the bundle and of myosin detachment, respectively. We take $\gamma_b = \gamma_m = \gamma$ for simplicity. The velocities of right- and left-oriented filaments and of myosin clusters are given by $v_r$, $v_l$, and $v_m$, respectively. $n_r$, $n_l$, and $n_m$ are the respective sources of right- and left-oriented filaments and myosin. These sources originate from the actin network and attached myosin clusters of the rear edge: forward translocation leads to these molecules' effective incorporation into the bundle. Since the density of F-actin near the rear edge is assumed constant, the total source of F-actin is also taken as constant along the bundle: $n_r(x) + n_l(x) = \text{const}$. Similarly, the myosin source is assumed constant. These sources may change in time, depending on how quickly the rear edge advances, but we neglect this possible time dependence for the sake of simplicity. Note that (4.1)–(4.3) assume that the average sizes of both the actin filaments and the myosin clusters are constant.

Though the total actin source is constant, the polarity of the F-actin in the bundle can be graded. Indeed, Svitkina et al. [32] observed that at the right (left) edge of the bundle most filaments were oriented to the right (left), while in the middle the polarity was equally mixed. The predominantly barbed-end growth near the leading edge may explain this graded polarity [19]. Because filaments do not change orientation after they are capped, the concave shape of the lamellipodial front would lead to the majority of the filaments at the right (left) side of the cell to be oriented to the right (left). Thus, filament polarization may depend on the leading edge shape; however, for simplicity we assume that the number of the right- (left-) oriented filaments increases linearly to the right (left). Hence,

$$(4.4) \qquad n_r = n_0 \frac{x + L}{L}, \quad n_l = n_0 \frac{L - x}{L}, \quad -L \le x \le L,$$

where $n_0$ is the average F-actin source.

Constitutive relations for the actin and myosin velocities stem from the following model (Figure 3). We assume each multiple motor domain bound in a myosin cluster attaches transiently and with equal probability to any actin filament within the 1-D bundle in the vicinity of this cluster, generating a constant average force $F_m$. We neglect a possible force-velocity relationship by assuming that all the motors operate near stall. Furthermore, we assume that myosin density, and not F-actin length, is the limiting factor in force generation. So the total force density exerted by myosin at $x$ is $F_m m(x)$. This force is distributed proportionally between right- and left-oriented filaments. Because myosin motors are barbed-end directed and equal to $F_r = -F_m m(x) r(x)/(r(x) + l(x))$ $(F_l = F_m m(x) l(x)/(r(x) + l(x)))$, the force on the right- (left-) oriented filaments is directed to the left (right) (Figure 3). We can find the corresponding force per right or left filament, $F_r/r$ and $F_l/l$, respectively, as well as the corresponding velocities, assuming there is an effective viscous resistance to filament movement (Figure 3):

$$(4.5) \qquad v_r = \frac{F_r}{\zeta_a r} = -\frac{F_m m}{\zeta_a (r + l)}, \qquad v_l = \frac{F_l}{\zeta_a l} = \frac{F_m m}{\zeta_a (r + l)},$$

with $\zeta_a$ representing the effective viscous drag coefficient. Physically, this resistance stems from breaking transient crosslinked bonds between the bundled filaments and

network filaments and adhesions. Similarly, the force applied to a myosin cluster is equal to $-(F_r + F_l)$, and its corresponding velocity is

$$(4.6) \qquad v_m = -\frac{F_r + F_l}{\zeta_m m} = \frac{F_m}{\zeta_m} \frac{r - l}{r + l},$$

with $\zeta_m$ representing the effective viscous drag coefficient per myosin. The corresponding absolute value of the total contractile force density is given by the sum:

$$(4.7) \qquad F_{net} = |F_r| + |F_l| + |F_r + F_l| = F_m m \left( 1 + \frac{|r - l|}{r + l} \right).$$

We substitute (4.4)–(4.6) into (4.1)–(4.3). Taking into account that the submodel variables have the scales $r \sim l \sim n_0/\gamma_b$, $m \sim n_m/\gamma_m$, $x \sim L$, and $t \sim 1/\gamma_b$, and rescaling the equations using these scales, we obtain the following nondimensional system of equations $(-1 \le x \le 1)$:

$$(4.8) \qquad \frac{\partial r}{\partial t} = (x + 1) - r + \epsilon_1 \frac{\partial}{\partial x} \left( \frac{mr}{r + l} \right),$$

$$(4.9) \qquad \frac{\partial l}{\partial t} = (1 - x) - l - \epsilon_1 \frac{\partial}{\partial x} \left( \frac{ml}{r + l} \right),$$

$$(4.10) \qquad \frac{\partial m}{\partial t} = 1 - m - \epsilon_2 \frac{\partial}{\partial x} \left( \frac{r - l}{r + l} m \right).$$

(We keep the same notations for the nondimensional and dimensional variables.) From the rescaling, we obtain two important nondimensional parameters: $\epsilon_1 = (n_m/n_0) \cdot (F_m/\zeta_a)/(L\gamma)$ and $\epsilon_2 = (F_m/\zeta_m)/(L\gamma)$. The first parameter has the meaning of the characteristic actin velocity scaled by the product of the bundle size and disassembly rate. The second parameter similarly has the meaning of characteristic myosin velocity scaled by the product of the bundle size and disassembly rate. The observed velocities are on the order of $0.1\,\mu\text{m/sec}$, while the corresponding scales are on the order of $1\,\mu\text{m/sec}$. As a result $\epsilon_1 \ll 1$ and $\epsilon_2 \ll 1$.

In this limit, the steady-state solutions of (4.8)–(4.10) can be found using singular perturbation theory:

$$(4.11) \qquad r \approx x + 1, \quad l \approx 1 - x, \quad r + l \approx 2, \quad m \approx 1, \quad F_{net} \sim 1 + |x|.$$

These approximate analytical solutions do not take into account the respective behaviors of the actin and myosin densities and velocities in the boundary layers of the width $\sim \epsilon_1, \epsilon_2$. Their boundary layer behaviors, which can be found using the boundary conditions $r(1) = l(-1) = 0$ and $m(0) = 1/(1 + \epsilon_2)$, are the exponential decrease of the actin densities to zero and almost no change of myosin density (Figure 4). In the composite model of the whole lamellipodium, we neglect this boundary layer behavior because there are large, peculiar adhesions at the edges of the bundle [34]. Actin-myosin interactions with these adhesions are unclear; thus, for the sake of simplicity, we use the approximate solutions (4.11) in the multiscale computations.

The equation $F_{net} \sim 1 + |x|$ is the key result of this section. It implies that the net force applied to the F-actin network and adhesions at the rear of the lamellipodium grows linearly with distance from the center (Figures 4 and 5). This effect can be understood qualitatively as follows. At the center, on average, myosin clusters do not move because they apply equal and opposite forces to equal numbers of oppositely
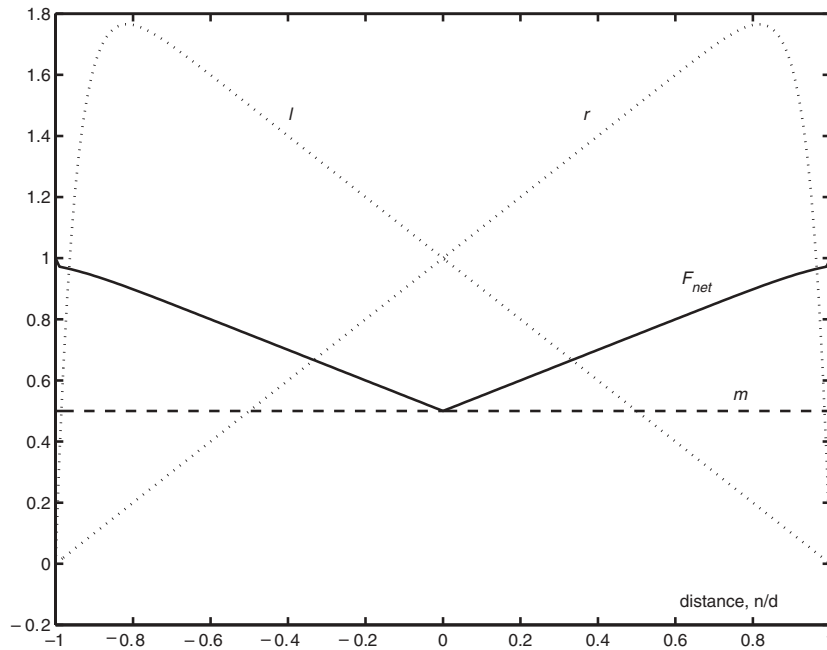
FIG. 4. *Stationary distributions of the right- and left-oriented actin filament densities (dotted) and of myosin density (dashed) predicted by the model of the 1-D actin-myosin bundle. The resulting magnitude of the force density applied to the actin network at the rear of the lamellipodium is shown with the solid line.*
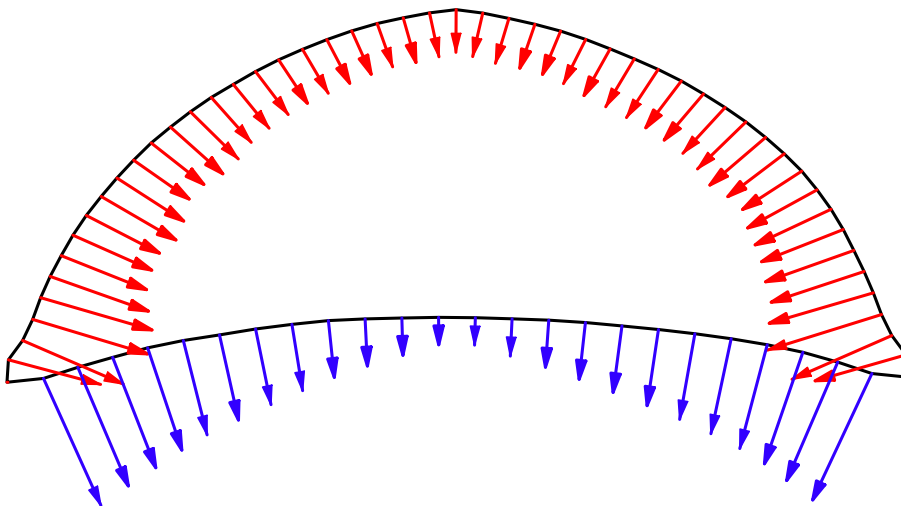


FIG. 5. *The lamellipodial domain and forces are plotted in a late stage of computation, when the shape and movement of the fragment are steady and stable. The bottom arrows show the contractile forces generated by the actin-myosin contraction at the rear edge; the top arrows show the elastic deformation (traction) forces at the leading edge. The traction forces applied to adhesions at the rear boundary are locally equal in magnitude but directed oppositely to the contractile forces. The sum of the traction forces applied by the cell to the substratum is equal to zero.*

oriented bundle filaments. As a result, the contractile stress per myosin cluster is equal to *half* the number of myosin heads multiplied by the force per head. On the other hand, at the sides, *all* myosin heads pull the polarized bundle filaments in a single direction. Thus, the contractile stress per myosin cluster at the sides is equal to the *total* number of myosin heads multiplied by the force per head (Figure 3).

Note that the model predicts the net inward flux of F-actin in the bundle $\sim (v_l l - v_r r) \sim -x$, which increases linearly from the center to the sides. This prediction can be tested in the future. The model also predicts the slow outward myosin drift. Such drift is not experimentally observed; therefore, the model may need revisions in the future.

**5. 2-D elastic model of lamellipodial actin network.** Following [4], we treat the lamellipodium as a thin 2-D elastic plate. However, we do not assume the distributed active contractile stress of [4] but instead localize that stress to the rear boundary. We model the corresponding linear elastic problem [16] using in-plane stress and strain as variables. We solve this problem for the two unknown components of the displacement vector, using a potential energy approach [16]. The potential energy, $\Pi$, of a linear elastic body is given by

$$(5.1) \qquad \Pi = \frac{1}{2} \int_\Omega \mathrm{Tr}(\sigma \epsilon) \, d\Omega - \int_\Gamma \mathbf{u} \cdot \mathbf{T} \, d\Gamma, \qquad \sigma = \mathbf{Y} \cdot \epsilon.$$

In (5.1), Tr means trace, $\sigma$ is the stress tensor, $\epsilon$ is the strain tensor with components $\epsilon_{ij} = 0.5(\partial u_i / \partial x_j + \partial u_j / \partial x_i)$, and $\mathbf{u}(\mathbf{x})$ is the displacement vector. $\Omega$ denotes the lamellipodial domain; $\Gamma$ denotes the rear boundary. $\mathbf{Y}$ is the so-called stiffness matrix; its elements are computed using values of Young's modulus and the Poisson ratio. Young's modulus determines the order of magnitude of the elastic deformations in the lamellipodium which develop in response to contractile forces. The traction forces $\mathbf{T}$ are applied to the rear boundary of the domain. We specify the boundary condition of zero displacement on the leading edge. The unique solution of this problem corresponds to the minimum of the potential energy functional (5.1) [16].

*Force balance at the rear boundary.* In the model introduced in the previous section, we implicitly assume that myosin heads develop sliding forces only by interacting with bundle filaments. Those heads which interact with network filaments do not generate active forces but instead act as crosslinks. These crosslinks are similar to the crosslinks between bundle and network filaments (Figure 3). (Indeed, myosin clusters do not contract the lamellipodial network away from the rear bundle [32].) The forces applied to network filaments through these crosslinks pull the network filaments into the bundle (Figure 3). These forces break the crosslinks and the network filaments, pulling them into the antiparallel bundle configuration [23].

Note that in the previous section we did not analyze the orientation of the contractile forces. We assume the contractile elements are almost parallel to the rear edge (Figure 3). Some contractile elements apply all myosin-generated stress to the F-actin network. These stresses break the network filaments and crosslinks but do not result in a traction force. We assume other contractile elements are linked transiently to both the F-actin network and the weak adhesions at the rear edge (Figure 3). These elements generate an oppositely oriented traction force applied to the substratum. At the same time, they create a local force which is applied to the actin network on the average normal to the rear boundary. The magnitude of the force is proportional to (4.11). Thus, the myosin-generated force at the rear boundary results in an effective force that pulls the lamellipodial network F-actin backwards into the bundle. This

force is locally normal to the rear edge (the bottom arrows in Figure 5). Hence the lamellipodium is elastically deformed, which, in turn, generates the traction force at the leading edge (the top arrows in Figure 5). The geometric sum of the traction forces applied to the substratum at the leading edge and at the rear edge (the top arrows, opposite to the bottom arrows in Figure 5, respectively) is equal to zero.

The following force balance argument underlies the assumptions made about the rear boundary position. Let us denote by $F_n$ the magnitude of the force per unit length which is normal to the rear boundary. $F_n$ pulls the network backward. Due to force balance, an equal and opposite force, denoted here by $F_a$, is pulling the weak adhesions forward. $F_a$ is a function of the local rate of advancement of the rear edge, $v$: $F_a = F_a(v) = F_n$. The rate of advancement depends on how fast the actin network is broken down by the contractile force; thus $v$ is a function of the local network density, $f$, and of the magnitude of the force: $v = v(f, F_n)$. Therefore, the two equations $F_a(v) = F_n$ and $v = v(f, F_n)$ locally determine $f$ and $v$. In the model we assume that, in the range of relevant parameters, the adhesion force is almost independent of the velocity. We also assume that the density, $f_{cr}$, at which the network breaks is almost independent of the rate of breaking. (Physically, both of these assumptions can be justified when a constant number of molecular links (adhesion links in the first case and actin crosslinks in the second case) are made per unit time, deformed, and broken before spontaneous dissociation. In this case, the total average force is velocity independent [22].) Because of these two assumptions, in the model (i) the local adhesion force is velocity independent; (ii) the density at the rear edge is equal to $f_{cr}$; and (iii) the rate of advancement of the rear edge is determined effectively not by the forces but by the rate of network disassembly. In the future, we will test more realistic and complex molecular models of the force balance at the rear edge.

**6. 2-D convection-reaction-diffusion model of actin transport.** One of the important features of rapid keratocyte migration is the steady and effective recycling of actin [24, 27]. As the F-actin network depolymerizes throughout the lamellipodium, G-actin assembles into F-actin along the leading edge, requiring a rapid, steady, forward transport of G-actin. Simple diffusion may be largely responsible for this transport [24], but some directional transport due to convection in the cytoplasm (possibly observed indirectly in [37]) might also play a role. Mathematically, this actin transport determines $a(\mathbf{x})$, the value of G-actin concentration, along the front which then modifies the protrusion rate, ultimately regulating leading edge shape.

In [24] we analyzed a detailed 1-D model of the lamellipodial actin transport. We omitted the fluid flow, which is essentially a 2-D effect. Here we consider, for the first time, the 2-D G-actin transport. This analysis is useful, even without modeling the lamellipodial shape, because relevant experimental data emerges and requires theoretical interpretation [35, 33].

For simplicity, we omit here some of the reactions considered in [24], namely the fast ADP-ATP and ADF/cofilin-profilin exchanges on G-actin. We consider the case when concentrations of thymosin and profilin (see section 2) are significant, resulting in almost all the G-actin being bound to either thymosin or profilin [24]. The corresponding 2-D densities are denoted by $b(\mathbf{x}, t)$ and $a(\mathbf{x}, t)$. These densities obey the following reaction-diffusion-convection equations:

$$(6.1) \qquad \frac{\partial b}{\partial t} = -k_1 b + k_2 a + D\Delta b - \nabla \cdot (\mathbf{V}_c b),$$

$$(6.2) \qquad \frac{\partial a}{\partial t} = k_1 b - k_2 a + \gamma_l f + D\Delta a - \nabla \cdot (\mathbf{V}_c a).$$

In (6.1) and (6.2), $k_1$ and $k_2$ are the effective rates of the thymosin-profilin exchange reactions [24], $D$ is the diffusion coefficient, and $\mathbf{V}_c(\mathbf{x}, t)$ is the velocity of the fluid phase of cytoplasm in the cell coordinate system. The term $\gamma_l f(\mathbf{x}, t)$ describes the source of G-actin from the F-actin; density $f(\mathbf{x}, t)$ depolymerizes with constant rate $\gamma_l$. The F-actin density dynamics are described by the equation

$$(6.3) \qquad \frac{\partial f}{\partial t} = -\gamma_l f.$$

The boundary conditions for this model include no flux of G-actin-thymosin at all boundaries of the lamellipodium, as well as no flux of G-actin-profilin at the rear edge. At the front edge, G-actin-profilin polymerizes onto F-actin barbed ends requiring the corresponding boundary condition of G-actin-profilin flux (left-hand side) to be equal to the rate at which G-actin-profilin assembles onto the filament tips (right-hand side):

$$(6.4) \qquad ([-D(\nabla a) + \mathbf{V}_c a] \cdot \mathbf{n})(\mathbf{x}) = -\frac{V(\mathbf{x})f(\mathbf{x})}{\delta\nu}.$$

Here $\mathbf{n}$ is the unit normal vector to the boundary and $\nu$ is a geometric dimension converting factor [24].

Finally, to find the velocity of the fluid phase of cytoplasm, we solve the equation for D'Arcy flow [36]

$$(6.5) \qquad (\mathbf{V}_c - \mathbf{V}_f) = -\frac{K}{\phi\eta}\nabla P, \quad \phi \approx 1 - 0.1f, \quad K \approx \frac{d^2\phi^3}{(1-\phi)^2},$$

coupled with the incompressibility condition:

$$(6.6) \qquad \nabla \cdot [\mathbf{V}_c\phi + \mathbf{V}_f(1-\phi)] = 0.$$

$\mathbf{V}_f$ is the velocity of F-actin in the moving lamellipodium coordinate system; $\eta$ is the water viscosity; $K$ is the F-actin permeability; $\phi$ is the porosity; $d$ is the actin filament diameter; $P$ is the hydrostatic pressure; and the F-actin density $f$ is scaled so that its value at the front center of the lamellipodium is equal to 1. The boundary condition represents the cell membrane's impermeability to water [13]. Equation (6.5) is valid in the limit of low Reynolds numbers characteristic of intracellular biological processes [36]; it says that the effective drag between the cytoskeletal network and fluid is linearly proportional to the corresponding velocity difference. Expression $(\phi\eta/K)$, derived and discussed in [36], is the corresponding effective drag coefficient. Furthermore, this effective drag is created by and is equal to the pressure gradient. The F-actin retrograde flow physically generates the pressure defined in (6.5). This pressure is ultimately powered by myosin action and is computed implicitly from the incompressibility condition (6.6), as is usual in the hydrodynamics of incompressible fluid.

**7. Simulations of the finite element model of the motile lamellipodial fragment.** The model is characterized by dimensional parameters listed in Table 2. The values of some of these parameters (such as $\delta$, $k_{on}$, $k_1$, $k_2$, $k_1'$, $k_2'$, $\eta$, $d$, and $\nu$) are well known from the literature. The values of the parameters $n_m$, $n_0$, and $\epsilon_{1,2}$ do not affect the model behavior. The F-actin disassembly rate, $\gamma_l$, is estimated in [24] from the experimental data. The characteristic size of the lamellipodium, $L$, is known from multiple observations. The actin and myosin disassembly rates in the rear bundle, $\gamma_f$ and $\gamma_m$, respectively, are unknown. The values assumed are an order of magnitude
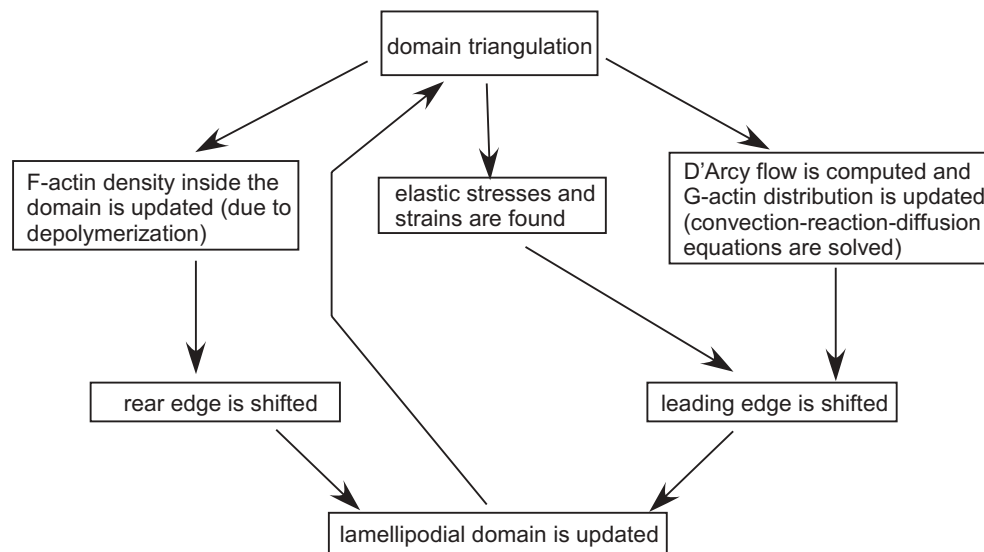
Fig. 6. *Diagram illustrating the computational procedure at each simulation step.*

higher than the F-actin disassembly rate in the lamellipodium, which is explained by the mechanical breaking of the cytoskeleton by myosin-generated forces at the rear. This is reasonable and does not affect model behavior, as long as the actual values are not more than an order of magnitude higher.

The order of magnitude of the diffusion coefficient, $D$, is known (see the relevant discussion in [24]). The force constants $F_0$ and $F_{cr}^0$ are unknown. We chose the values listed in Table 2 to be on the order of characteristic values of traction forces [26]. Characteristic actin densities $f_{cr}$ and $f_0$ are also unknown. We chose their values to be on the order of characteristic F-actin densities described in [24]. Exact values of parameters $D$, $F_0$, $F_{cr}^0$, $f_{cr}$, and $f_0$ do not affect the model behavior qualitatively but do determine the exact shape and rate of movement of the lamellipodium. More research is necessary to investigate the model dependence on these parameters' values.

The Young's modulus in the model is 10 kPa [28]. In order for the model to be valid, this modulus has to be high enough (higher than 1 kPa) to ensure that the deformations are small enough for the linear model. Recently, a number of studies reported smaller numbers (0.01–0.1 kPa); however, controversy exists about when these measurements are valid. The value of the Poisson ratio characterizes the relationship between local deformations in perpendicular directions. Its exact value does not affect the results much, as long as it is between 0.1 and 0.45. We take the value to be 0.25.

The complexity of the interactions and the geometry preclude direct mathematical analysis of the model; therefore, we use a finite element model to investigate the dynamics described above. A good elementary introduction to the finite element method can be found in [31]. Here we will present the method using a more heuristic approach.

In the numerical simulations we implemented the following scheme, illustrated in Figure 6:

• At each iteration step, we specify the lamellipodial domain for triangulation by an ordered set of boundary point coordinates along with boundary markers denoting the type of the boundary point (belonging to either the leading or rear edge).

An ordered array of edges of the boundary is provided. The triangulation procedure is performed using the external `Triangle` package written by J. R. Shewchuk. This package is called in a manner which prevents creation of extra boundary points other than those supplied to the package. We also specify the maximal area of the created triangles. Typically, there are several hundreds of triangular elements.

- We solve the ordinary differential equation (6.3) for F-actin density on the triangular mesh.
- We solve the discretized elasticity problem (4.11), (5.1) using the external `LASPack` package written by Tomáš Skalický. This package is designed for the solution of sparse linear systems and adopted for singular systems. We choose the conjugate gradient squared method with preconditioning because it also works for nonsymmetric systems. The computed displacement vector solution is substituted into the original system. The error norm is checked against a prescribed accuracy.
- We solve the D'Arcy flow equations (6.5)–(6.6) using `Femlab`.
- We solve the reaction-diffusion-convection equations (6.1), (6.2), and (6.4) using `Femlab`.
- Using the value of the elastic force induced at the front edge by the contractile force generated at the rear edge, we determine the positions of the ends of the leading and rear edges, $x_r$ and $x_l$. Namely, the end points of the domain are those at which the force reaches the critical value $F_{cr}$. These points are then points at which the velocity of front edge protrusion is zero and the F-actin density is equal to $f_{cr}$. The lateral sides are assumed to be parts of the front edge. The right lateral side is a single segment of the front edge connecting points with the same value of $x$-coordinate; the $y$-coordinates are determined from the intersection of the straight line $x = x_r$ with the updated front and rear edges. The right lateral side is first. The same procedure is followed for the left lateral side which is the last segment of the front edge. The intersections are found using linear interpolation or extrapolation procedures.
- The position of the rear edge is determined by the curve at which actin density reaches its critical value $f(\mathbf{x}) = f_{cr}$. The curve is found as an ordered set of points belonging to the sides of the triangular elements. The procedure begins with the determination of the triangular element having one side at the front edge on which the critical density is reached. Then the point at this side with $f(\mathbf{x}) = f_{cr}$ is found using linear interpolation. The linear interpolation is used to find a similar point on the other side of this triangle. This second point also belongs to an adjacent triangle. This procedure is repeated until a point belonging to the front edge is found. Thus, an ordered set of points representing a new rear edge is constructed. The fixed number $N = 24$ of rear edge points is distributed equidistantly over the new rear edge; this makes the shift of the edge done as a shift of each boundary point on the edge.
- The leading edge motion depends on elastic deformation forces as described above. The elastic forces $F_e(\mathbf{x})$ exerted on a boundary segment $\Delta l$ are computed using the stress tensor $\sigma$ (which is constant inside each triangular element) and the relation $F_e = -\sigma \mathbf{n} \Delta l$, where $\mathbf{n}$ is the unit normal vector to the boundary. The local leading edge protrusion velocity is determined using formulae (3.1)–(3.3). The shift of the front edge is found as $\Delta \mathbf{x} = V \Delta t$. After the shift is made, the fixed number $N = 51$ of front edge points is distributed equidistantly over the new front edge. The F-actin density in the vicinity of the leading edge is found using (3.4). We create a boundary of the new domain connecting the front and rear edges. A rectangle bounding the new domain is found. We compute the instant velocity of cell motion as the ratio of the bounding rectangle center shift $\Delta \mathbf{x}$ to the time step: $\mathbf{V} = \Delta \mathbf{x} / \Delta t$.
- We choose a length scale equal to the typical size of the lamellipodial frag-

ment: $L = 10\,\mu$m. We scale the Young's modulus to the traction force scale using the formulation which converts the stress tensor components through the strain tensor in the plane-stress case. Our effective 2-D model was produced by reducing the full three-dimensional (3-D) model with the assumption of constant lamellipodial thickness $(0.2\,\mu$m). The characteristic value of traction force per unit length is $\sim 1\,$nN$/\mu$m$^2$, and the scaled value of the Young's modulus is 10. The traction force applied at the rear boundary is scaled with respect to $1\,$nN$/\mu$m. The characteristic migration speed is $V = 0.25\,\mu$m/sec, so we choose a time scale of $40\,$sec $= L/V$.

The program is written as a combination of `C`, `Matlab`, and `Femlab` codes. The simulations are run on a desktop PC. The dynamic behavior of the model can best be appreciated by viewing the movie that can be downloaded from http://www.math. ucdavis.edu/~mogilner/CompKerat1.mpg. The simulations that produced this movie take about 10 minutes of computational time. The "virtual lamellipodium" was simulated for 20 time units; this corresponds to 7.5 minutes of real time. The scaling is chosen so that the cell travels roughly one cell's body length over each time unit. Thus the simulations capture cell translocation over significant distance (of the order of 10 body lengths). Figure 7 shows frames from this movie.

We start the simulations with an initial perfect crescent shape (Figure 7(a)). The initial area of the lamellipod is a few-fold less than the equilibrium area, so the leading edge expands rapidly (Figure 7(b)). The rear edge rapidly "catches up" with the expanding leading edge, and the forces generated at the rear (Figure 5) stop the expansion of the leading edge (Figure 7(c)). Finally, after 4–5 time units ($\sim 3$ minutes of real time) the equilibrium shape evolves (Figure 7(d)), and the fragment moves steadily and persistently without changing shape (for $\sim$ 4–5 minutes of real time, traveling close to 10 cell body lengths).

The computed hydrostatic pressure and velocity of the cytoplasmic fluid phase are shown in Figure 8. The F-actin moves backward relative to the leading edge; this movement then "drags" the fluid phase backward, creating the computed pressure gradient, from the rear to the front. Closer to the center of the lamellipodial domain, the F-actin drag overcomes the pressure gradient, and the fluid moves backward. Meanwhile, closer to the sides, the F-actin density is low, and the pressure pushes the fluid forward. This creates "eddies," shown in Figure 8. This flow pattern assists in the recycling of G-actin across the lamellipodium, although the simulations show its relative importance is low. Further studies are needed to investigate the effect of the flow at different geometries and diffusion coefficients.

Note that, from both the simulations and the scaling in formula (6.5), the model predicts the order of magnitude of the hydrostatic pressure is $P \sim LV_f\eta\phi^2/d^2 \sim 0.1\,$pN$/\mu$m$^2$. This value is orders of magnitude lower than either the characteristic actin-myosin contractile stress or the effective protrusion force per unit area. Hence it seems the mechanical role of the hydrostatic pressure in thin lamellipodial protrusions is negligible.

Figure 9 illustrates the computed distribution of the sum of G-actin-thymosin and G-actin-profilin densities. Due to G-actin assembly at the leading edge, a gradient of G-actin develops. The resulting density at the rear is about two times larger than the density at the front. This gradient leads to the effective diffusive delivery of G-actin to the leading edge. Note that G-actin density at the front is a little lower than that at the sides; however, the force stalling protrusion at the sides overcomes the graded influence of G-actin density on protrusion there.

The model simulates a broad range of features of the lamellipodial motility. Most importantly, it reproduces the observed, persistent, steady-state movement and its
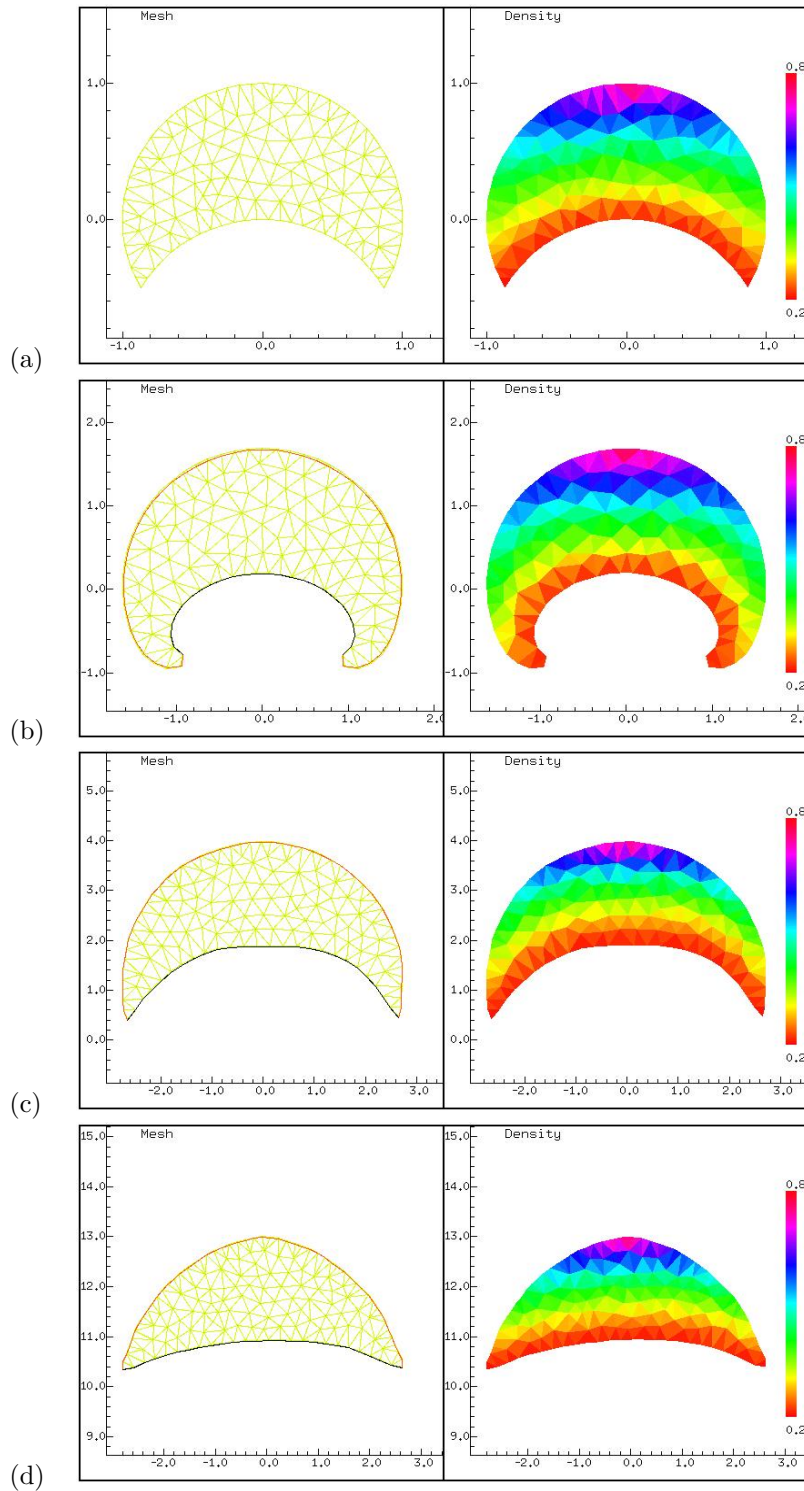
Fig. 7. *Four consecutive snapshots* (a)–(d) *of the computed lamellipodial domains with triangular mesh (left) and F-actin density (right) are shown. x- and y-coordinates are plotted in the lab coordinate system.* (a) $t = 0$; (b) $t = 1.5$ *time units;* (c) $t = 4.5$ *time units;* (d) $t = 13.5$ *time units.*
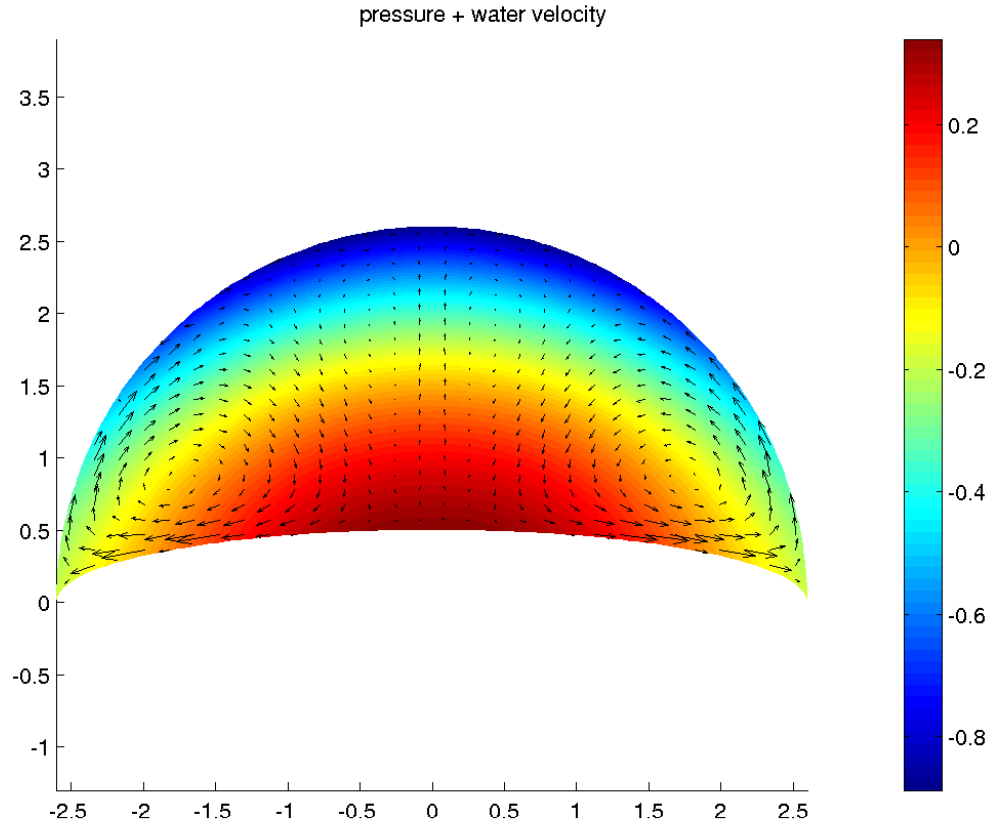
FIG. 8. *Computed pressure (nondimensional) and velocity field of the cytoplasmic fluid phase in the lamellipodial domain.*

characteristic crescent shape. We tested the stability of the model to the choice of the initial shape and found that the model generally produces the same final shape despite these differing initial shapes. We are unable to reproduce this result from an initial disc-shaped fragment [34] because of computational difficulties: before the stability break, the discoid shape of the lamellipodial fragment crucially depends on the distributed 2-D myosin contraction and F-actin retrograde flow, which we cannot yet handle numerically. Nevertheless, the model is valid because it can reproduce *locally stable* cell movements. Global bistability of the lamellipod underlying the experiment reported in [34] is more challenging to simulate. Modeling this experiment is one of our future priorities. The F-actin density distribution also agrees with observations [32]. The G-actin distribution and fluid cytoplasmic velocities are model predictions that can be tested in the future.

**8. Simulations of the turning lamellipodial fragment response to local perturbations of actin transport.** The model allows us to not only simulate the steady, stable lamellipodial locomotion but also some transient complex cell movements. For example, when caged thymosin was photoreleased at the left side of a keratocyte lamellipodium, the cell's left edge stopped and the cell "pivoted" around its left side, making a half-turn [29]. The authors of [29] suggest that this behavior could be explained if (i) the local concentration of the polymerization-able G-actin
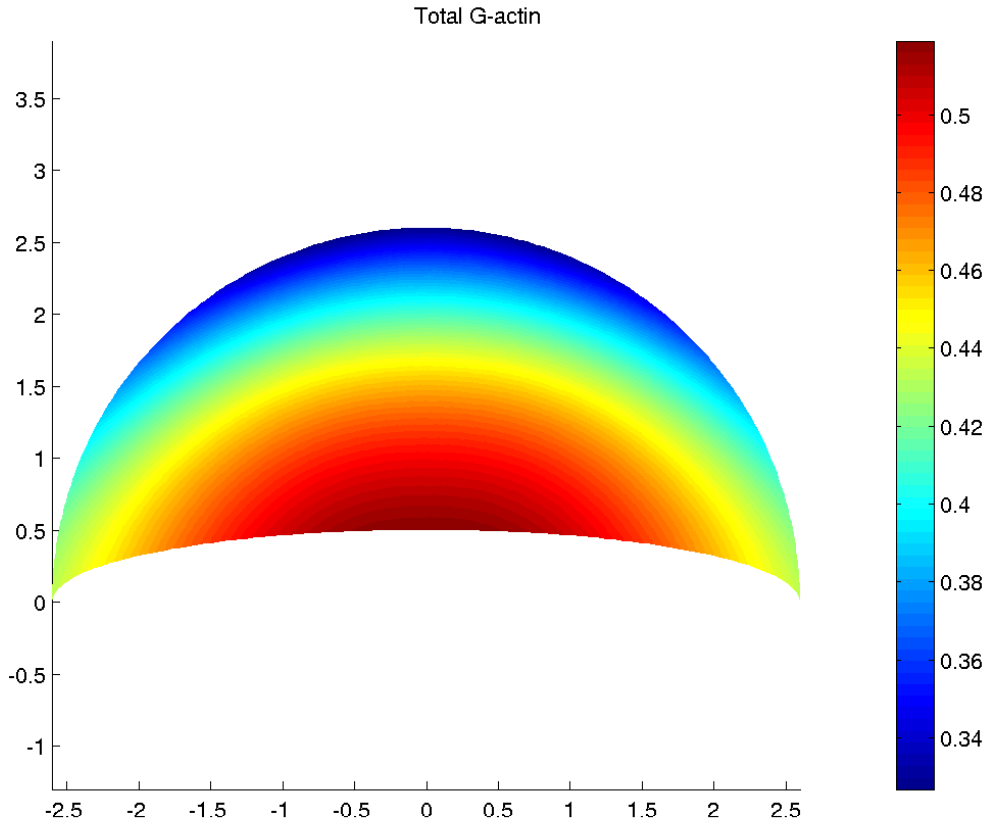
FIG. 9. *Computed G-actin distribution in the lamellipodial domain.*

was arrested by the released thymosin and (ii) low local G-actin concentration inhibits both protrusion of the leading edge and contraction of the rear edge but not the adhesion. The idea is that the center and right side of the leading edge would continue to advance. Since the cell cannot diverge from its left side, it pivots. We test this hypothesis using the model.

In order to do this testing, we first have to change the actin turnover submodel as follows. In section 6, we implicitly assumed that both concentrations of profilin and thymosin are higher than the G-actin concentration. In this situation, release of more thymosin would have only a minor effect on G-actin dynamics. In this section, for simplicity and clarity, we assume that the profilin concentration is negligible and the thymosin concentration is less than that of G-actin. In this case we denote the densities of G-actin-thymosin, G-actin, and thymosin by $b$, $a$, and $\beta$, respectively. They are governed by the following equations:

$$(8.1) \qquad \frac{\partial b}{\partial t} = -k_1' b + k_2' a\beta + D\Delta b - \nabla \cdot (\mathbf{V}_c b),$$

$$(8.2) \qquad \frac{\partial a}{\partial t} = k_1' b - k_2' a\beta + D\Delta a - \nabla \cdot (\mathbf{V}_c a),$$

$$(8.3) \qquad \frac{\partial \beta}{\partial t} = k_1' b - k_2' a\beta + D'\Delta \beta - \nabla \cdot (\mathbf{V}_c \beta).$$

The diffusion and convection terms in (8.1)–(8.3) have the same meaning as the corresponding terms in section 6; $k_1'$ is the rate of dissociation of thymosin from G-actin; $k_2'$ is the rate of association of thymosin and G-actin. For a moment, we neglect sources and sinks of G-actin and consider the no flux boundary conditions for all variables on all boundaries. In this case the following conservation laws are valid:

$$\int_\Omega (a(\mathbf{x}) + b(\mathbf{x}))\, d\mathbf{x} = a_0 \int_\Omega d\mathbf{x} = \text{const}, \qquad \int_\Omega (a(\mathbf{x}) + \beta(\mathbf{x}))\, d\mathbf{x} = \beta_0 \int_\Omega d\mathbf{x} = \text{const},$$

where $a_0 > \beta_0$ are the conserved total densities of actin monomers and thymosin molecules.

In the relevant range of model parameters [24], $k_1 \ll k_2'(a_0 - \beta_0)$, thymosin binds tightly to G-actin. As a result the concentration of free thymosin molecules is very small. In this limiting case, the characteristic concentration scales are as follows:

$$b \sim \beta_0, \quad a \sim (a_0 - \beta_0), \quad \beta \sim (k_1 b_0)/(k_2'(a_0 - \beta_0)), \quad \beta \ll a, b.$$

We use these scales, along with $1/k_1'$ as a time scale and $L$ as the spatial scale, to nondimensionalize, obtaining the following system of equations:

$$(8.4) \qquad \frac{\partial b}{\partial t} = -b + a\beta + \lambda_1 \Delta b - \nabla \cdot (\mathbf{V}_c b),$$

$$(8.5) \qquad \frac{\partial a}{\partial t} = \lambda_2(b - a\beta) + \lambda_1 \Delta a - \nabla \cdot (\mathbf{V}_c a),$$

$$(8.6) \qquad \frac{\partial \beta}{\partial t} = \frac{1}{\epsilon}(b - a\beta) + \frac{D'}{D}\lambda_1 \Delta \beta - \nabla \cdot (\mathbf{V}_c \beta).$$

The nondimensional parameters are

$$\lambda_1 = \frac{D}{L^2 k_1'} \sim 0.1, \qquad \lambda_2 = \frac{\beta_0}{(a_0 - \beta_0)} \sim 1,$$

$$\epsilon = \frac{k_1'}{k_2'(a_0 - \beta_0)} \sim 0.01, \qquad \frac{D'}{D} \sim 10, \qquad v_c = \frac{V_c}{L k_1'} \sim 0.01.$$

(We keep the same notations for the nondimensional and dimensional variables.) In this limit, the concentration of free thymosin equilibrates rapidly with local G-actin and G-actin-thymosin and $\beta \approx b/a$. The equations for the concentrations of G-actin and G-actin-thymosin then uncouple and become very simple:

$$(8.7) \qquad \frac{\partial b}{\partial t} \approx D\Delta b - \nabla \cdot (\mathbf{V}_c b), \qquad \frac{\partial a}{\partial t} \approx D\Delta a - \nabla \cdot (\mathbf{V}_c a).$$

In the simulations we solve only the second of the pair of (8.7) for the free G-actin density instead of simulating the submodel of section 6. We use the boundary condition given in section 6 for this density and add the source of G-actin from disassembling F-actin. We also modify the magnitude of the traction actin-myosin force (4.11) at the rear boundary according to the following formula:

$$(8.8) \qquad \tilde{F}_{net}(\mathbf{x}) = F_{net}(\mathbf{x}) \cdot \frac{a(\mathbf{x})}{a_{aver}}, \qquad a_{aver} = \int_\Omega a(\mathbf{x})\, d\mathbf{x}.$$

The underlying rationale is the possibility that, at very low G-actin concentration, enhanced depolymerization of the actin bundle depletes the bundle to the point where a low number of actin filaments could become the force limiting factor.

The results of the simulations of this modified model can best be appreciated by viewing the movie that can be downloaded from http://www.math.ucdavis.edu/~mogilner/turn.mpg. The simulations that produced the movie take around 10 minutes of computational time. The "virtual lamellipodium" was simulated for 10 time units (corresponding to approximately 4 minutes of real time) over which the "virtual lamellipodium" turns at a roughly right angle. Note that in the experiment [29] the corresponding turn took a similar amount of time. Figure 10 shows frames from this movie.

Initially, thymosin is released, and the free G-actin concentration drops at the left (Figure 10(a)). The leading edge protrusion and contraction at the left are significantly inhibited. Because both protrusion and retraction at the right are changed little, the cell starts to "pivot" (Figure 10(b)–(c)). Diffusion and convection redistribute the free G-actin, while the cell makes a quarter-turn (Figure 10(b)–(c)). The simulation results agree qualitatively with the observations [29].

**9. Discussion.** The general principles of cell crawling have been established for some time [1]; however, many details remain elusive. Broadly speaking, two questions that need to be resolved are the following: (1) What is the physical nature and the molecular basis of protrusion, retraction, and adhesion? (2) How are these three processes coordinated to achieve the observed shapes and movements of crawling cells? These questions have been subjects of biophysical studies and mathematical modeling for some time, but there have been only a few attempts to connect the molecular and cellular levels of description to the whole crawling cell [8, 4].

Here we have developed a 2-D multiscale model of the actin-myosin system that generates movement in simple crawling cells. Flatness of the keratocyte's lamellipodium makes this 2-D modeling adequate and relieves us from the very challenging task of simulating 3-D cells. We propose that protrusion is made possible by actin polymerization and growth of uncapped barbed ends at the leading edge. The effective protrusion rate is graded by the strength of adhesion along the leading edge; this strength is, in turn, graded by the contractile forces transmitted from the rear via the elasticity of the lamellipodial actin network. These forces are generated at the rear by actin-myosin sliding. Depolymerization of the lamellipodial actin network weakens the lamellipodium and provides the source of G-actin. As a result, myosin collapses the actin network into the actin bundle and generates the contractile forces which slide the actin filaments from the sides to the center of the bundle. G-actin is transported to the front of the lamellipodium by diffusion and convection. The model accounts for the steady fan-like shape of the lamellipodium, as well as its persistent "gliding."

The model we present here identifies the minimal processes that underlie self-organization of the lamellipodium and provides a dynamic mechanism for the kinematic GRE model. The main contribution of our multiscale model is that it demonstrates for the first time that protrusion and adhesion localized to the front and regulated mechanically by the myosin generated forces localized to the rear and chemically by actin turnover and transport are sufficient to explain the fan-like lamellipodial shape. Furthermore, quantitative estimates show that the observed concentrations, reaction rates, and forces can explain the lamellipodial shape and movement not just qualitatively but also quantitatively.

Predictive capacity of the model of the whole lamellipodium is limited. The problem is that a few crucial assumptions of the model are plausible but not proven. Such assumptions include (i) adhesion, rather than membrane resistance, as the limiting
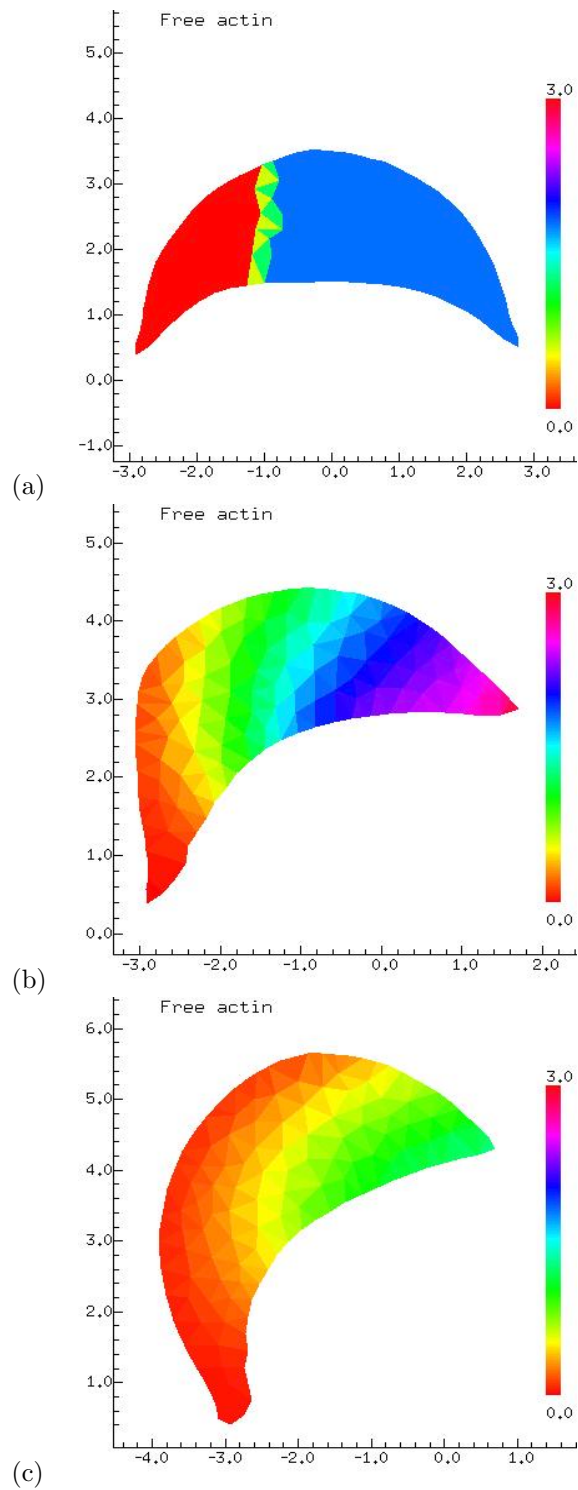
(a)

(b)

(c)

Fig. 10. *Three consecutive snapshots* (a)–(c) *of the computed turning lamellipodial domain with free G-actin density are shown. x- and y-coordinates are plotted in the lab coordinate system.* (a) $t = 0$; (b) $t = 5$ *time units;* (c) $t = 10$ *time units.*

factor for protrusion; (ii) concentrations of myosin, nucleation (Arp2/3), and adhesion molecules as the factors limiting lamellipodial area; and (iii) contractile forces at the rear as governors of the adhesion at the front. Detailed biophysical research needs to verify these assumptions or suggest alternates. Other model limitations stem from simplifications chosen to avoid challenging mathematical and computational complexities at this early stage of modeling cell movements. For example, we have (i) considered the lamellipodial network as an elastic (rather than viscoelastic) plate, (ii) neglected the retrograde flow of the actin network, and (iii) concentrated actin-myosin sliding at the very rear of the lamellipodium.

The value of the model, besides its theoretical reproduction of lamellipodial motility, is in the examination of a minimal set of assumptions that are sufficient for a quantitative description of cell crawling. In subsequent publications, we will systematically change the model assumptions in order to examine impacts of alternative sets of assumptions on the shape and movement of the "virtual lamellipodium." For example, the number of uncapped barbed ends might be a limiting factor for protrusion [12]. We are presently performing numerical experiments on how including barbed ends in the model affects lamellipodial shape. We will also gradually improve the modeling technique to allow simulations of more realistic models. Finally, we will continue to coordinate our modeling efforts with experimental studies. In particular, transient lamellipodial shapes, similar to those illustrated in Figures 7 and 10, will be compared to data. These future developments of our model will make it predictive and provide a conceptual framework for evaluating many aspects of cell locomotion quantitatively.

Our general modeling approach is applicable to a number of other crawling cells such as fibroblasts, nerve growth cones which are more important for biomedical applications than keratocytes. All of these cells use an actin-myosin lamellipodial protrusion-contraction-adhesion cycle for motility. Therefore, the computational diagram in Figure 6 is applicable. However, the specifics of the computational steps can differ significantly depending on cell type. For example, significant stress fiber contractility, as well as complex adhesion dynamics, would need to be modeled to capture the fibroblasts' irregular movements. Filopodial protrusion is essential in describing nerve growth cone advancement. As far as there is sufficient data to make realistic model assumptions, theoretical studies of more cell types are possible. Some other cells, such as neutrophils [13], move differently and thus require different approaches. It is also necessary to include the cell body in the model. At present, the nature of the interactions between the lamellipodium and the cell body remains elusive. If, as some observations indicate [34], the cell body is but a passive cargo, then the corresponding modeling is easy, straightforward, and similar to that in [4]. However, if the forces [2] and actin exchange [33] between the cell body and the lamellipodium are active and nontrivial, the model would need to be changed significantly, though the general modeling formalism of this paper would still be applicable.

## REFERENCES

[1] M. ABERCROMBIE, *The Croonian lecture,* 1978. *The crawling movement of metazoan cells*, Proc. Roy. Soc. London Ser. B, 207 (1980), pp. 129–147.

[2] K. I. ANDERSON AND R. CROSS, *Contact dynamics during keratocyte motility*, Curr. Biol., 10 (2000), pp. 253–260.

[3] J. E. BEAR, T. SVITKINA, M. KRAUSE, D. A. SCHAFER, J. J. LOUREIRO, G. A. STRASSER, I. V. MALY, O. Y. CHAGA, J. A. COOPER, G. BORISY, AND F. B. GERTLER, *Antagonism between Ena/VASP proteins and actin filament capping regulates fibroblast motility*, Cell, 109 (2002), pp. 509–521.

[4] D. BOTTINO, A. MOGILNER, T. ROBERTS, M. STEWART, AND G. OSTER, *How nematode sperm crawl*, J. Cell Sci., 115 (2002), pp. 367–384.

[5] D. BRAY, *Cell Movements*, Garland, New York, 2002.

[6] D. A. CALDERWOOD, A. HUTTENLOCHER, W. B. KIOSSES, D. M. ROSE, D. G. WOODSIDE, M. A. SCHWARTZ, AND M. H. GINSBERG, *Increased filamin binding to beta-integrin cytoplasmic domains inhibits cell migration*, Nat. Cell Biol., 3 (2001), pp. 1060–1068.

[7] K. A. DEMALI, C. A. BARLOW, AND K. BURRIDGE, *Recruitment of the Arp2/3 complex to vinculin: Coupling membrane protrusion to matrix adhesion*, J. Cell Biol., 159 (2002), pp. 881–891.

[8] P. A. DIMILLA, K. BARBEE, AND D. A. LAUFFENBURGER, *Mathematical model for the effects of adhesion and mechanics on cell migration speed*, Biophys. J., 60 (1991), pp. 15–37.

[9] E. EVANS AND K. RITCHIE, *Strength of a weak bond connecting flexible polymer chains*, Biophys. J., 76 (1999), pp. 2439–2447.

[10] C. G. GALBRAITH AND M. P. SHEETZ, *Keratocytes pull with similar forces on their dorsal and ventral surfaces*, J. Cell Biol., 147 (1999), pp. 1313–1324.

[11] M. E. GRACHEVA AND H. G. OTHMER, *A continuum model of motility in ameboid cells*, Bull. Math. Biol., 66 (2004), pp. 167–193.

[12] H. P. GRIMM, A. VERKHOVSKY, A. MOGILNER, AND J.-J. MEISTER, *Analysis of actin dynamics at the leading edge of crawling cells: Implications for the shape of keratocyte lamellipodia*, Eur. Biophys. J., 32 (2003), pp. 563–577.

[13] M. HERANT, W. A. MARGANSKI, AND M. DEMBO, *The mechanics of neutrophils: Synthetic modeling of three experiments*, Biophys. J., 84 (2003), pp. 3389–3413.

[14] I. KAVERINA, O. KRYLYSHKINA, AND J. V. SMALL, *Regulation of substrate adhesion dynamics during cell motility*, Int. J. Biochem. Cell Biol., 34 (2002), pp. 746–761.

[15] K. KRUSE AND F. JULICHER, *Actively contracting bundles of polar filaments*, Phys. Rev. Lett., 85 (2000), pp. 1778–1781.

[16] L. LANDAU AND E. LIFSHITZ, *The Theory of Elasticity*, Butterworth-Heinemann, Boston, 1995.

[17] J. LEE, A. ISHIHARA, J. THERIOT, AND K. JACOBSON, *Principles of locomotion for simple-shaped cells*, Nature, 362 (1993), pp. 467–471.

[18] J. LEE AND K. JACOBSON, *The composition and dynamics of cell-substratum adhesions in locomoting fish keratocytes*, J. Cell Sci., 110 (1997), pp. 2833–2844.

[19] I. V. MALY AND G. G. BORISY, *Self-organization of a propulsive actin network as an evolutionary process*, Proc. Natl. Acad. Sci. USA, 98 (2001), pp. 11324–11329.

[20] A. MOGILNER AND G. OSTER, *Cell motility driven by actin polymerization*, Biophys. J., 71 (1996), pp. 3030–3045.

[21] A. MOGILNER AND G. OSTER, *The physics of lamellipodial protrusion*, Eur. Biophys. J., 25 (1996), pp. 47–53.

[22] A. MOGILNER, M. MANGEL, AND R. J. BASKIN, *Motion of molecular motor ratcheted by internal fluctuations and protein friction*, Phys. Lett. A, 237 (1998), pp. 297–306.

[23] A. MOGILNER, E. MARLAND, AND D. BOTTINO, *A minimal model of locomotion applied to the steady "gliding" movement of fish keratocyte cells*, in Pattern Formation and Morphogenesis: Basic Processes, H. Othmer and P. Maini, eds., Springer, New York, 2001, pp. 269–294.

[24] A. MOGILNER AND L. EDELSTEIN-KESHET, *Regulation of actin dynamics in rapidly moving cells: A quantitative analysis*, Biophys. J., 83 (2002), pp. 1237–1258.

[25] A. MOGILNER AND G. OSTER, *Polymer motors: Pushing out the front and pulling up the back*, Curr. Biol., 13 (2003), pp. R721–R733.

[26] T. OLIVER, M. DEMBO, AND K. JACOBSON, *Separation of propulsive and adhesive traction stresses in locomoting keratocytes*, J. Cell Biol., 145 (1999), pp. 589–604.

[27] T. D. POLLARD AND G. BORISY, *Cellular motility driven by assembly and disassembly of actin filaments*, Cell, 112 (2003), pp. 453–465.

[28] C. ROTSCH, K. JACOBSON, AND M. RADMACHER, *Dimensional and mechanical dynamics of active and stable edges in motile fibroblasts investigated by using atomic force microscopy*, Proc. Natl. Acad. Sci. USA, 96 (1999), pp. 921–926.

[29] P. Roy, Z. Rajfur, D. Jones, G. Marriot, L. Loew, and K. Jacobson, *Local photorelease of caged thymosin beta4 in locomoting keratocytes causes cell turning*, J. Cell Biol., 153 (2001), pp. 1035–1048.

[30] R. Sambeth and A. Baumgaertner, *Locomotion of a 2-D keratocyte model*, J. Biol. Systems, 9 (2001), pp. 201–219.

[31] G. Strang, *Introduction to Applied Mathematics*, Wellesley-Cambridge Press, Wellesley, MA, 1986.

[32] T. Svitkina, A. Verkhovsky, K. McQuade, and G. Borisy, *Analysis of the actin-myosin* II *system in fish epidermal keratocytes: Mechanism of cell body translocaction*, J. Cell Biol., 139 (1997), pp. 397–415.

[33] P. Valloton, A. Ponti, C. M. Waterman-Storer, E. D. Salmon, and G. Danuser, *Recovery, visualization, and analysis of actin and tubulin polymer flow in live cells: A fluorescent speckle microscopy study*, Biophys. J., 85 (2003), pp. 1289–1306.

[34] A. Verkhovsky, T. Svitkina, and G. Borisy, *Self-polarization and directional motility of cytoplasm*, Curr. Biol., 9 (1999), pp. 11–20.

[35] N. Watanabe and T. J. Mitchison, *Single-molecule speckle analysis of actin filament turnover in lamellipodia*, Science, 295 (2002), pp. 1083–1086.

[36] C. Zhu and R. Skalak, *A continuum model of protrusion of pseudopod in leukocytes*, Biophys. J., 54 (1988), pp. 1115–1137.

[37] D. Zicha, I. M. Dobbie, M. R. Holt, J. Monypenny, D. Y. Soong, C. Gray, and G. A. Dunn, *Rapid actin transport during cell protrusion*, Science, 300 (2003), pp. 142–145.